

Conceptual stage separation from widebody subsonic carrier aircraft for space access

U. Mehta

unmeel.b.mehta@nasa.gov

J. Bowles, S. Pandya and J. Melton

NASA Ames Research Center
Moffett Field
California
USA

L. Huynh, J. Kless and V. Hawke

Science and Technology Corporation
Moffett Field
California
USA

ABSTRACT

Stage separation is a critical technical issue for developing two-stage-to-orbit (TSTO) launch systems with widebody carrier aircraft that use air-breathing propulsion and launch vehicle stages that use rocket propulsion. During conceptual design phases, this issue can be addressed with a combination of engineering methods, computational fluid dynamics simulations, and trajectory analysis of the mated system and the launch vehicle after staging. The outcome of such analyses helps to establish the credibility of the proposed TSTO system and formulate a ground-based test programme for the preliminary design phase. This approach is demonstrated with an assessment of stage separation from the shuttle carrier aircraft. Flight conditions are determined for safe mated flight, safe stage separation, and for the launch vehicle as it commences ascending flight. Accurate assessment of aerodynamic forces and moments is critical during staging to account for interference effects from the proximities of the two large vehicles. Interference aerodynamics have a modest impact on the separation conditions and separated flight trajectories, but have a significant impact on the interaction forces.

NOMENCLATURE

Symbols

\vec{a}	acceleration vector, ft/sec ²
\vec{e}	unit vector
g	gravitational acceleration, ft/sec ²
h	altitude, ft
l	length, ft
m	mass, lbm
r	distance between launcher CG and mated CG, ft
A_x	axial force, lbf
D	drag force, lbf
K	thousand
L	lift force, lbf
M	freestream Mach number
M	moment, lbf-ft
N_a	normal force at aft strut, lbf
N_f	normal force at forward strut, lbf
V	velocity, ft/sec
W	weight, lbm
X	horizontal distance, ft
Y	transverse distance, ft
Z	vertical distance, ft
α	angle-of-attack of the carrier aircraft, deg
θ	incidence angle between the carrier aircraft and the launch vehicle, deg
ω	rotational velocity
Δ	delta

Acronyms

CFD	Computational Fluid Dynamics
CG	Centre of Gravity
DARPA	Defense Advanced Research Projects Agency
DOF	Degree of Freedom
HLS	Horizontal Launch Study
HOTOL	Horizontal Take-Off and Landing
LEO	low-Earth orbit
LOX	liquid oxygen
MAKS	Multipurpose Aerospace System
NASP	National Aero-Space Plane
OMS	Orbiter Manoeuvring System
PD	Point Design
POST	Programme to Optimise Simulated Trajectories
SABRE	Synergetic Air-Breathing Rocket Engine
SCA	Shuttle Carrier Aircraft
SST	Shear Stress Transport
SSTO	Single Stage to Orbit
TSTO	Two Stage to Orbit

Abbreviations

deg	degree
ft	feet
in	inches
Isp	specific impulse, sec
lbm	pound mass
mph	miles per hour
psf	pounds per square foot
ref	reference quantity
sec	seconds
ΔZ	vertical separation distance from launch vehicle baseline location

1.0 INTRODUCTION

The history of transportation teaches us that excellence in transportation leads to economic, security, and exploration advantages and that progress in transportation is made by revolutionary changes in modes of propulsion. The development of the Western United States in the 19th century was made possible when steam engine-driven train systems replaced horse-driven Conestoga wagons. A significant advance in transportation took place when power from horses was replaced with power from internal combustion engines. Transportation with aircraft in the 20th century changed the aviation paradigm when jet-powered aircraft replaced propeller driven aircraft. Such revolutionary propulsion advances transform transportation and surpass non-propulsive advances such as swept wings, stressed skin metal structures, retractable landing gear, flaps, variable-pitch propellers, and low-drag engine cowlings. When chemical rocket engines are complemented with air-breathing engines for space access, we have a revolutionary propulsion system for space access.

A paradigm change in the transportation of medium-weight payloads to low-Earth orbit (LEO) with respect to affordability, reliability, safety, resiliency, and operational responsiveness can be made only if existing chemical rocket engines are partially replaced with air-breathing propulsion. Affordability addresses reusability, the annual flight rate, and commercial airline industry practices. All-rocket engine-powered systems cannot meet the criteria of resiliency and operational responsiveness, but air-breathing propulsion powered systems can do so. Based on the aforementioned criteria, we can realise this paradigm change with either a single-stage-to-orbit (SSTO) spaceplane that uses air-breathing propulsion during atmospheric flight, or with a two-stage-to-orbit (TSTO) system that uses air-breathing propulsion on the carrier aircraft stage and rocket propulsion on the launch vehicle stage.

Two of the principal technical challenges with the TSTO concept are placing the launch vehicle at appropriate flight conditions to begin its ascent after separation from the carrier aircraft, and safely separating the two large vehicles in midair. In this study, we address these challenges during the system's conceptual design phase using engineering methods, computational fluid dynamics (CFD) simulations, and separation trajectory analyses. We illustrate this approach by investigating the feasibility of satisfactory stage separation from the Shuttle Carrier Aircraft (SCA) for space access.

The remainder of this introduction provides an overview of previous TSTO system developments and stage separation tests, and presents the *raison d'être* for this study.

In 1959, the need for a recoverable booster system to provide routine access to space led to the recoverable orbital launch system (aerospace plane) programme in the United States⁽¹⁾. The US Air Force emphasised TSTO concepts as first-generation options, based on guidance from the Air

Force Scientific Advisory Board and other *ad hoc* committees. In November 1965, after intensive study, review, and evaluation, the TSTO concept with an air-breathing first stage and a conventional rocket launch vehicle second stage was selected as the preferred approach. In 1970, when the US Space Shuttle Phase B award began, NASA and contractors were generally unanimous in considering fully reusable TSTO concepts as the most viable launch approach⁽²⁾.

In 1938, Sänger and Bredt designed an SSTO, sled-launched, rocket-powered, winged boost-glider⁽³⁾ called the Rocket Spaceplane. This design evolved from the Silbervogel (Silver Bird) that Sänger developed in the early 1930s. The Rocket Spaceplane design had to give way to the constraints of technology, however, and was replaced with a TSTO system dubbed Sänger I in the early 1960s. Around 1987, Sänger II – consisting of a turboramjet-powered, Mach 6.7 carrier aircraft and a rocket-propelled launch vehicle – was proposed⁽⁴⁾.

In 1966, the D-21 unmanned drone was initially designed to be launched at Mach 3+ from a pylon on top of its M-21 carrier aircraft. The D-21 ramjet engine was started before launch. The D-21 was successfully launched three times with the M-21 in a 0.9g dive. During the fourth and final launch, the D-21 was separated in a level, 1g flight configuration. After 2 or 3 seconds, the drone was not able to penetrate the shock wave coming off the M-21 and the engine un-started. The D-21 then impacted the M-21 where the forward fuselage attaches to the wing root, causing the M-21 nose to pitch-up, breaking the aircraft in two⁽⁵⁾.

In 1977, staging and free-flight tests of *Enterprise* lightweight, 122ft, non-spaceflight-worthy shuttle orbiter – were conducted with the SCA-905 as part of the Approach and Landing Tests programme. The free-flight phase test programme was performed to learn how the Space Shuttle would handle in low-speed flight and landing attitudes. Five free flights were conducted. During the first three tests, *Enterprise* remained fitted with its aerodynamic tail cone, which was intended to reduce drag when mounted on the SCA during flight. For the final two tests, the tail cone was removed and the orbiter was in its full operational configuration with dummy main engines and Orbiter Manoeuvring System (OMS) pods. *Enterprise* was jettisoned using explosive bolts at altitudes ranging from 19,000 to 26,000ft and launch speeds ranging from 278 to 310mph⁽⁶⁾.

In the 1980s, the Antonov An-225 Mriya was designed to carry the Buran orbiter piggyback. It was considered as a carrier aircraft for three different Multipurpose Aerospace System (MAKS) configurations for space access⁽⁷⁾. The An-225 was also considered for air-launching of the interim-HOTOL⁽⁸⁾. Aircraft such as the SCA, B747-400F, B747-800F, and A380-800F were not designed to carry a launch vehicle. The An-225 Mriya is longer than the B747-800F by 25.43ft and can carry significantly heavier launch vehicles.

In 1993, the Rand Corporation believed that the US Air Force's TSTO choice in the 1960s was commendable and would be a strong contender for developing the X-30 spaceplane under the National Aero-Space Plane (NASP) programme⁽¹⁾. Later that year, after reviewing the status of the X-30, the US General Accounting Office recommended that single-stage-to-orbit (SSTO) concepts be re-examined as an approach to pursue⁽⁹⁾. In 1994, Ben Rich expressed that the X-30 is actually two separate concepts, one a rocket ship and the other an airplane, and said: "most likely, that particular twain shall never meet successfully."⁽¹⁰⁾ The proposed Synergetic Air-Breathing Rocket Engine⁽¹¹⁾ (SABRE) may turn out to be an exception to this pronouncement. Until then, TSTO system concepts will be pursued.

Efforts to develop a reusable, horizontal take-off TSTO system were restarted for Sänger II around 1987 and for NASA space access study⁽¹²⁾ in 1993. Since then, a few such TSTO system concepts have been conceptualised and studied. These efforts considered air-breathing propulsion on the carrier aircraft, which staged the piggybacked rocket-powered launch vehicle at a subsonic, a supersonic, or at a hypersonic Mach number.

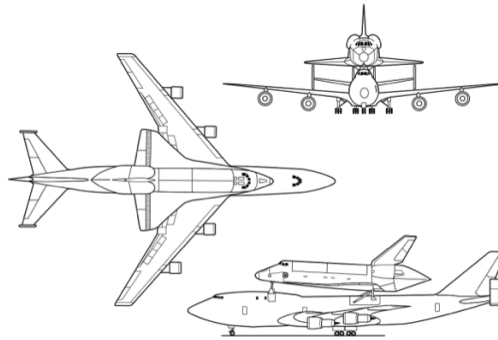


Figure 1. The SCA with shuttle orbiter.

In 2002, the first flight of WhiteKnightOne took place⁽¹³⁾. This carrier aircraft was specially designed to provide a high-altitude, airborne launch of SpaceShipOne. Subsequently, WhiteKnightTwo, or Eve, was developed as the mothership and launch platform for SpaceShipTwo and potentially for a launch vehicle with small-weight payload. In 2012, Stratolaunch Systems⁽¹⁴⁾ started developing an operational carrier—designed to carry a launch vehicle with medium-weight payload—without risk-reduction flight tests or an experimental/demonstration system.

In 2010, the DARPA-NASA Horizontal Launch Study (HLS) began to examine potential near-term concepts to deliver 15,000lbm payloads to LEO⁽¹⁵⁾. These concepts used existing carrier aircraft and launch vehicles modified with state-of-the-art systems and technologies. Three proposed operational concepts were based on the B747-400F aircraft as the air-breathing carrier stage. Two other proposed flight demonstration system concepts used the SCA-905 aircraft as the carrier stage. The latter aircraft is a modified B747-100. Key changes in the B747-100 aircraft included the installation of two additional vertical stabilisers, one on each end of the standard horizontal stabiliser, to enhance directional stability⁽¹⁶⁾ (Fig. 1) and new bulkheads to strengthen the fuselage at critical stress areas.

Among the B747 family of aircraft, the SCA is the least capable as a carrier aircraft and the B747-800F is the best suited to launch medium-weight payloads. The B747-800F is 250ft 2in long, whereas, the SCA and the B747-400F are 231ft 10in. Also, the B747-800F has the potential to carry appreciably heavier launch vehicles than the B747-400F.

The separation of a top-mounted vehicle from a carrier aircraft has been demonstrated, for example, with the Short-Mayo Composite, the Junker/Focke-Wulf Composite, and the Space Shuttle and SCA-905 combination at subsonic Mach numbers; and with the D-21 drone and the M-21 aircraft at supersonic Mach numbers. Whatever the staging Mach number, a system-level analysis is mandatory irrespective of whether a well-known or new staging technique is contemplated because of safety concerns. Such an analysis determines the final design, as well as safe staging envelope and conditions. The Antonov An-225 aircraft was specifically designed to carry MAKS-OS, MAKS-T, or MAKS-M piggyback and to stage the carried system with a well-known technique. In this case, a system-level analysis led, for example, to two vertical tails on the aircraft.

The principal technical uncertainty for any launch vehicle piggybacked on a carrier aircraft is launch vehicle separation, including both separation mechanisms and separation aerodynamics. To resolve this uncertainty, the stage separation analyses presented in this paper were performed for the HLS. Although the HLS did not use such analyses for selecting their five recommended concepts, the results presented in this paper led the HLS to identify this unaddressed technical uncertainty as one the most important risks for their concepts⁽¹⁵⁾.

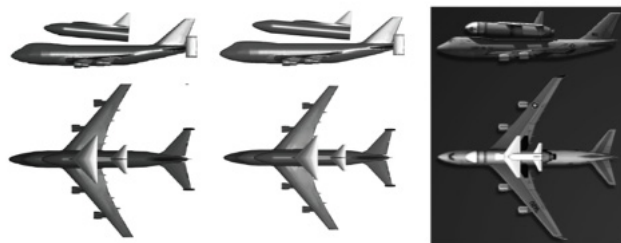


Figure 2. Two TSTO concepts considered in this study with the SCA-911 aircraft (left and centre) and the HLS PD-3 TSTO concept with the B747-400F aircraft (right).

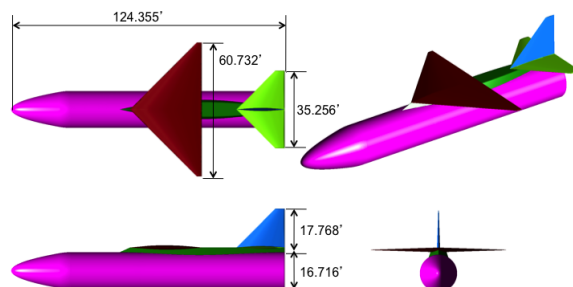


Figure 3. Launch vehicle with 47ft payload fairing.

An assessment must be done to determine whether a conceptual design is credible before determining whether the design is viable for its intended use. Only after satisfactory levels of design credibility and viability are achieved can sound strategic and policy decisions be made regarding further development phases. In this study, we performed such an assessment to suggest a viable launch configuration and separation mechanisms, and to determine whether the selected launch vehicle can be staged safely from the SCA-911 and achieve appropriate flight conditions to begin its powered ascent.

2.0 LAUNCHER CONFIGURATION

For this TSTO study, we investigated an SCA-911 carrier aircraft with two different sizes of launch vehicle stages. We chose the SCA-911, which is a modified B747-100SR, as the carrier aircraft because it offers a greater payload capability than the SCA-905. The length of the carrier aircraft (SCA-905 or SCA-911 and B747-400F) is 231ft 10in. The two launch vehicle stages considered in this study are a 107.4ft long vehicle with a 30ft payload fairing, and a 124.4ft long vehicle with a 47ft payload fairing. These were the dimensions that the HLS initially chose for its launch vehicle concepts. Figure 2 shows the TSTO concepts considered in this study and one of the Point Design (PD) concepts (PD-3) recommended by the HLS. Figure 3 shows one of the launch vehicle designs (with the 47ft payload fairing) studied herein.

The launch vehicle design used in this study has an ogive nose that transitions smoothly to the cylindrical main body of the launcher. The wing is located above the body with an attachment pylon. The wing and tail aerofoils have smooth leading edges and blunt trailing edges. This vehicle had a very high wing loading and a relatively low angle-of-attack at separation; that is, it could not generate significant normal load factors. Although additional aerodynamic improvements were

Table 1
Geometric characteristics of the launcher wing and tails and HLS PD-3 wing

Parameter	Wing	Tails (horizontal & vertical)	HLS PD-3 wing
Aspect ratio	3.5	2.7	3.5
Taper ratio	0.068	0.19	0.2
Leading edge sweep angle	45°	45°	36.4°
Planform area	1057ft ²	461ft ²	803ft ²
Thickness-to-chord ratio	0.06	0.06	0.1
Incidence angle	0°		5°

feasible and the launch vehicle with the rocket engine could have been considered, they were not essential for the main objective of this study, which was to investigate stage separation during the conceptual design phase.

The stage separation results presented herein helped to improve the aerodynamic design of the launchers recommended by the HLS. The HLS reduced the length of their initially selected launch vehicle and the launch vehicle wings were placed at 5° incidence. The longest launch vehicle recommended is 113.7ft in length (Fig. 2, PD-3). The geometric characteristics of the studied launcher wing and tail are presented in Table 1. The launch vehicle's centre of gravity is directly above the SCA's centre of gravity.

3.0 AERODYNAMICS

The level of fidelity that analytical tools must have depends upon the intended use of the analytical results. A successful separation of the launch vehicle from the top of a widebody carrier aircraft requires the two stages to separate without recontact. To evaluate whether the manoeuvre will be successful, we need to know the aerodynamic forces and moments on each stage. The level of aerodynamic analytical fidelity varies from Level 0 to Level 4 as described in Table 2. Forces and moments are traditionally obtained during the conceptual design phase using engineering-based 1970s Missile DATCOM^(17,18) methods. The HLS used these methods to achieve Fidelity Level 1 force and moment data for PD and flight test concepts. These methods are not accurate for considered vehicle geometries, however, and thus only provide ballpark estimates; they also cannot determine aerodynamic interaction effects between the carrier aircraft and the launch vehicle. A more recent, improved method is to use CFD to obtain the required aerodynamic forces and moments for specific design concepts during the conceptual design phase. The present study used CFD to achieve Fidelity Level 2 in assessing stage separation concepts.

Conceptual design CFD simulations help to identify key required measurements and formulate the test matrix developed with the design of experiments (DOE). Relevant test data from ground-based test facilities and Fidelity Level 4 analyses are necessary for preliminary design efforts.

Inviscid CFD simulations can be carried out cheaply and quickly for conceptual designs, and the affordability and speed of viscous (higher-fidelity) simulations are also improving due to faster computers and advanced analysis algorithms. One further advantage of using CFD to obtain forces and moments for stage separation problems is that one can account for proximity effects between the two stages.

Table 2
Fidelity of aerodynamic analysis (adapted from Ref. 15)

Fidelity level	Description
0	Scaled empirical.
1	Linear or impact methods with all empirical drag increments adjusted to level or higher; vehicle satisfies all takeoff and landing speeds, glide path, and runway length requirements.
2	Three-dimensional, inviscid (Eulerian) CFD with integral boundary layer or potential with semiempirical drag increments or thin-layer Navier-Stokes with semiempirical nonviscous drag increments; vehicle satisfies all takeoff and landing speeds, glide path, runway length, and longitudinal stability requirements.
3	Three-dimensional CFD with parabolised Navier-Stokes finite-difference/volume flowfield analysis and integral boundary layer analysis; vehicle satisfies all take-off and landing speeds, glide path, runway length, and longitudinal, lateral, and yaw stability requirements.
4	Three-dimensional CFD with full or thin-layer Navier-Stokes flowfield analysis including pressure feedback, and with shear stress effects computed directly; vehicle satisfies all takeoff/landing speeds, glide path, runway length, and longitudinal, lateral, and yaw stability requirements.

In this study, we used inviscid CFD analyses to generate aerodynamic databases for the two stages, both separately and in proximity to each other. We then used viscous CFD to spot-check the inviscid results and ensure that they are acceptable for the geometries and flight conditions being studied. Viscous CFD results were also used to determine drag increments between viscous and inviscid solutions. The incremental drag values were used in the engineering-based separation analysis and the trajectory analysis presented in Section 5 and Section 6, respectively. All CFD simulations were performed without considering flow through the engines. This simplification does not change the conclusions reached regarding interference effects and stage separation, because experimental drag coefficients were used to include the effect of flow through the carrier aircraft engines.

The required level of credibility for these CFD simulations depends upon how the results will be used. In this study, forces and moments are used to assess the conceptual viability of stage separation. Direct verification and circumstantial validation of simulated forces and moments were conducted. The achieved levels of CFD simulation credibility are satisfactory to assess the viability of stage separation from widebody aircraft during the conceptual design phase.

For the inviscid CFD simulations, Cart3D was used to compute the flow field^(19,20). Cart3D is a Cartesian, upwind code that solves the Euler equations using an explicit, multi-stage, Runge-Kutta time-stepping algorithm to drive the solution to a steady state. An optimally damped second-order scheme using five Runge-Kutta stages was used to compute the set of subsonic cases considered in this study⁽²¹⁾. The volume mesh generation algorithm takes the intersected surface triangulation as input, and generates an unstructured Cartesian mesh by subdividing the hexahedral cells of an initially uniform, coarse grid⁽²²⁾. The flow solver also uses multi-grid convergence acceleration to damp the high-frequency error modes. In the present computations, five levels of multi-grid were used.

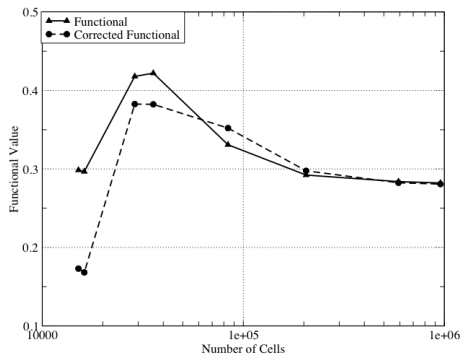


Figure 4. Functional values reach asymptotic levels as the number of cells is increased.

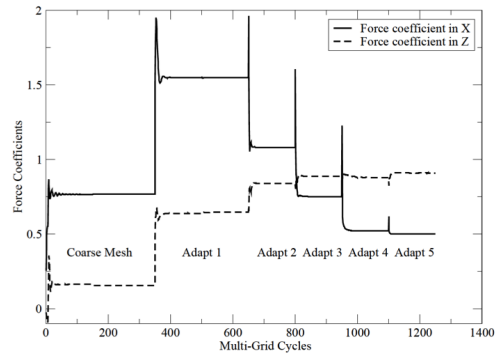


Figure 5. Convergence of forces and moment as the number of cells are increased.

Adjoint-based, automatic, adaptive mesh refinement was used to ensure the best possible mesh to generate sufficiently credible simulations for the purposes of this study⁽²³⁾. This procedure is intended to reduce the discretisation uncertainty in a chosen functional with each adaption of the mesh. A combination of lift and drag is specified as the adaptation functional and the associated uncertainty tolerance is specified. The adaptation process is started by computing a flow solution on a coarse mesh. The adjoint procedure is then used to compute an estimate of the error, i.e. uncertainty, in each cell of this mesh. Cells introducing large uncertainties are refined to minimise functional uncertainty. The flow solution is then recomputed on the adapted mesh. Repeated use of this process produces a sequence of adapted meshes. With each adaption cycle, the remaining numerical uncertainty in the simulated forces is reduced. The process is stopped either when the functional uncertainty tolerance is achieved or when the functional uncertainty does not decrease any more but fluctuates due to unsteady flow. Several adaption cycles later, a grid-converged solution is obtained on a flow-adapted mesh.

Five to eight adaptations were conducted for this study. An example is provided in Figs 4 and 5 for a mated TSTO system. Figure 4 shows the convergence of the functional and its adjoint-based correction as a function of the number of cells. As the number of cells increases with each adaptation cycle, the functional values converge. The uncertainty from the adjoint process is also used to correct the solution on the existing mesh. Note that as the mesh is adapted, the corrected functional is closer to the computed functional, indicating that the uncertainty has been reduced. Figure 5 also shows the history of the force coefficients as a function of the multi-grid cycle number. The jumps in forces correspond to mesh adaption. This figure shows that the change in force coefficients is smaller and smaller as the mesh is refined, indicating that the values of these coefficients are converging. Thus, this simulation verification effort leads to the desired level of numerical accuracy for the intended use of the computed forces and moments.

In the absence of test data for the present stage separation study, these forces and moments were 'validated' with circumstantial evidence. The Cart3D code with adjoint-based adaptive mesh refinement has been extensively used to study transonic and supersonic flows. Frequently, relevant aspects of Cart3D simulations have been validated with experimental data for the intended uses. For example, Cart3D simulations of a glide-back booster concept have been experimentally validated and shown to provide forces and moments that agreed very well with test data⁽²⁴⁾. Other validation examples include studies on low sonic-boom design concepts⁽²⁵⁻²⁷⁾. These studies focused on pressure signatures, which could adequately be simulated using Cart3D with adjoint-based mesh refinement.

Table 3**A verification study of Star-CCM+ forces and moments on a mated launch vehicle**

Volume cells	Lift, lbf	Uncertainty in lift	Drag, lbf	Uncertainty in drag	Moment, ft-lbf	Uncertainty in moment
6·600 x 10 ⁶	84,946		21,153		1,020,089	
10·700 x 10 ⁶	81,915	−3·57 %	20,421	−3·46 %	1,024,406	0·42 %
28·134 x 10 ⁶	83,227	−2·02 %	19,876	−6·04 %	987,281	−3·22 %

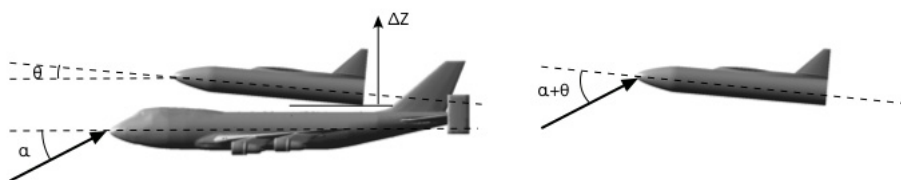


Figure 6. Co-ordinate system for the SCA and the launch vehicle in mated configuration (left) and the isolated launch vehicle (right).

For the present study, the Cart3D software was used to generate inviscid CFD simulations of each isolated stage at several angles-of-attack (α) to establish the baseline forces and moments. Simulations of the two bodies in proximity (in mated configuration) were then compared to the isolated results to obtain the proximity effects. The proximity effects were assessed for several separation distances and one incidence angle between the launch vehicle and the SCA. In order to assess the effect of the inviscid assumption, these simulation results were compared to a sampling of viscous results obtained using the commercial code Star-CCM+^(28,29). This code is widely used throughout the automotive and aerospace industries to provide aerodynamic estimations of complex configurations.

The Star-CCM+ simulations were conducted with the well-known k -omega shear stress transport (SST) turbulence model^(30,31). The transition from laminar flow to turbulent flow was not modeled. Approximately 6·6m unstructured finite-volume-based cells were used.

The grid-independence of the simulated force and moment results (moment computed at the aft attachment location) was assessed for a test condition (Mach = 0·8 and $\alpha = 8^\circ$). Table 3 shows the results of this verification study. It presents uncertainties in forces and moments determined with 6·6m cells as the number of cells is increased. The level of numerical uncertainty achieved is appropriate for a conceptual analysis study based on Fidelity Level 2 (Table 2).

Circumstantial evidence for credibility of the physics simulated by the Star-CCM+ code for the present study is provided by a recent validation study conducted for a high-lift NASA trapezoidal wing⁽³²⁾. Simulated force, moment, and surface pressure values for the trapezoidal wing agreed quite well with test data prior to stall, except pressure values very near the wing tip.

Figure 6 shows the co-ordinate system for the mated configuration and the isolated launch vehicle. As the figure shows, the angle-of-attack (α) is with respect to the body axis of the SCA, and the incidence angle (θ) is the angle between the body axis of the SCA and the body axis of the launch vehicle. Thus, when comparing cases, the mated configuration with angle-of-attack α and incidence angle θ is compared to the isolated configuration with an angle-of-attack of $\alpha + \theta$. The vertical separation distance between the upper surface of the SCA and the lowest point of the aft end of the launcher is 4·2ft.

Table 4
Cases for the isolated launch vehicle and isolated SCA

Code	Mach	A
Cart3D	0.6 & 0.8	0, 2, 4, 6, 8, 10, 12, & 14
Star-CCM+	0.6	0, 4, 5, 8, & 12

Table 5
Cases for the mated SCA and launch vehicle

Code	Mach	ΔZ ft	θ	α
Cart3D	0.6 & 0.8	0	2, 5, 8, 11	-4, 0, 3, 4 & 8
Cart3D	0.6 & 0.8	15, 30, 45, 100, & 200	8	0
Star-CCM+	0.6 & 0.8	0	0	5 & 8

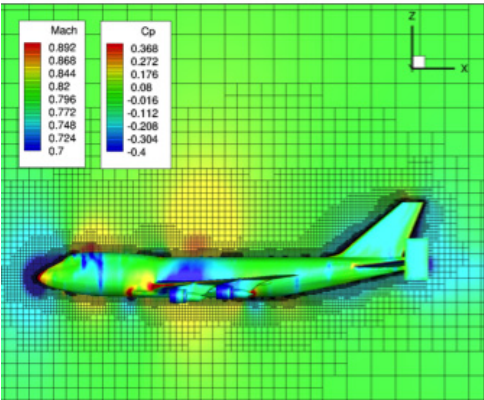


Figure 7. Cart3D Mach number contours on the symmetry plane and surface pressures on the isolated SCA ($M = 0.8$, $\alpha = 0$).

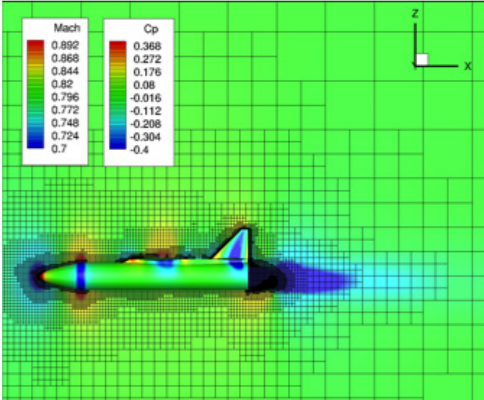


Figure 8. Cart3D Mach number contours on the symmetry plane and surface pressures on the isolated launcher ($M = 0.8$, $\alpha = 0$).

Tables 4 and 5 list the simulation cases performed for the isolated and mated configurations, respectively. In these tables, ΔZ is the vertical distance from the baseline location of the launch vehicle. Mach 0.6 and Mach 0.8 simulations were performed at altitudes of 20,000ft and 40,000ft, respectively.

Comparison of the mated and isolated vehicle cases provides a definitive assessment of the interference effects that the two vehicles have on each other's lift and drag when in close proximity. The resulting database also produces a lift value for the launch vehicle, which allows us to assess whether there is enough lift for the launch vehicle to separate on its own when the carrier is in straight, level flight.

First, results of the isolated stage simulations are discussed to assess the effect of the inviscid assumption. Next, the interference effects due to the two bodies flying in proximity are investigated on the SCA and on the launch vehicle. Finally, the ability of the launch vehicle to lift itself off the SCA is assessed.

Figures 7 and 8 show the results of one of the inviscid, isolated simulation cases for the SCA and launch vehicle, respectively. Both figures show Mach number contours in the flow field and pressure contours on the vehicle surface. Areas of particular interest in these images are the belly of the launch vehicle and the top of the SCA, where the pressures should change when the vehicles are in proximity to each other.

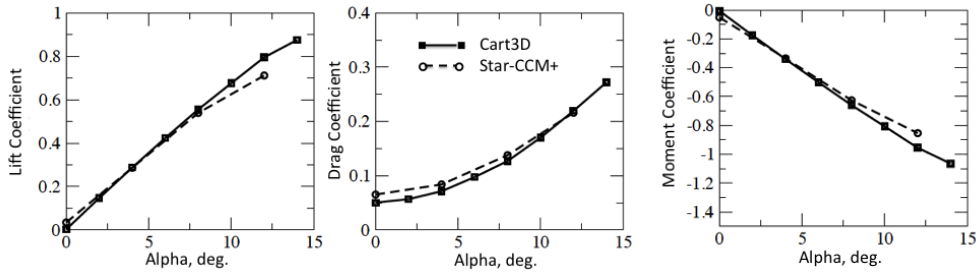


Figure 9. Comparison of forces and pitching moments computed with inviscid (Cart3D) and viscous (Star-CCM+) CFD solvers for the isolated launch vehicle (Mach 0.6 and 20,000ft altitude).

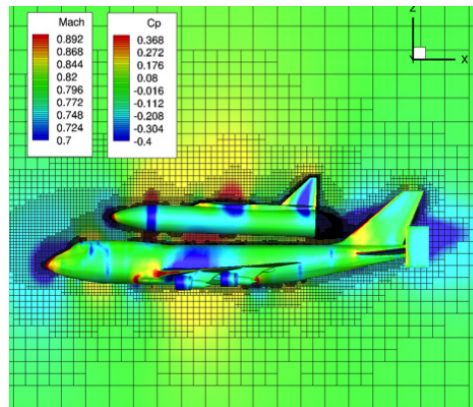


Figure 10. Cart3D Mach number contours and surface pressures for the mated configuration ($M = 0.8$, $\alpha = 0^\circ$, $\theta = 2^\circ$ and $\Delta Z = 0\text{ft}$).

Figure 9 shows the isolated inviscid and viscous coefficients of lift, drag, and pitching moment for the launch vehicle at Mach 0.6 as a function of angle-of-attack. The plots in this figure show that the inviscid computations are very close to the viscous results for reasonable values of angle-of-attack. Therefore, inviscid computations are appropriate to use for further analyses.

Figures 10, 11, and 12 show a progression of three incidence angles, with the SCA at a zero angle-of-attack, to assess the interference effects. The comparison shows that there is a significant interference effect when the two vehicles are near each other. When the two bodies are closest together at $\theta = 2^\circ$, there is a substantial low-pressure region on the belly of the launch vehicle due to the channeling effect between the two bodies. This effect is also seen at higher Mach numbers in that region, and in lower pressures on the SCA in the same vicinity. The effect is reduced with increasing θ , and the forces and moments will presumably return to the isolated-case values when the bodies are far enough apart. These conclusions are valid at free-stream Mach numbers 0.6 and 0.8. Also, the inviscid simulations compare very well with viscous simulations (Figs 11(b) and 12(b)).

The same interference effects can be seen in a plot of the coefficient of lift, drag, and pitching moment at Mach 0.8 and $\theta = 2^\circ$, as shown in Fig. 13. This figure shows the variation of forces and moments with respect to the angle-of-attack for the SCA, both in isolated and mated configuration. Only the forces and moments for the SCA are shown. It can be seen that, while there is little effect on the lift and pitching moments, the drag changes substantially due to the proximity effects. The same conclusions are drawn for the Mach 0.6 case.

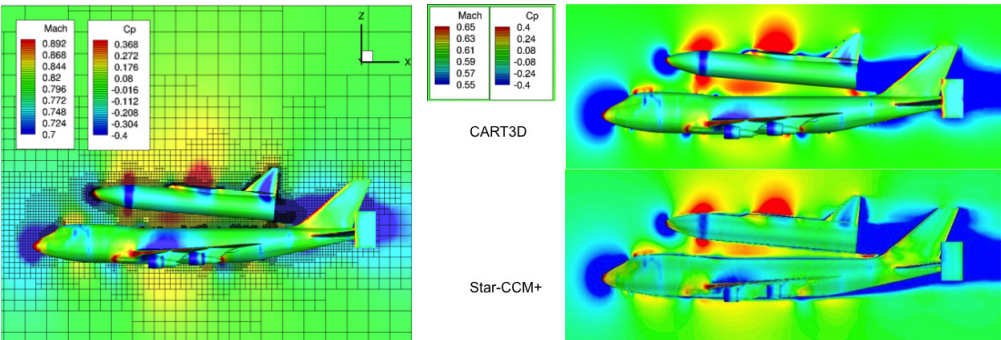


Figure 11(a). Cart3D Mach number contours and surface pressures for the mated configuration ($M = 0.8$, $\alpha = 0^\circ$, $\theta = 5^\circ$ and $\Delta Z = 0$ ft).

Figure 11(b). Mach number contours and surface pressures for the mated configuration ($M = 0.6$, $\alpha = 0^\circ$, $\theta = 5^\circ$ and $\Delta Z = 0$ ft).

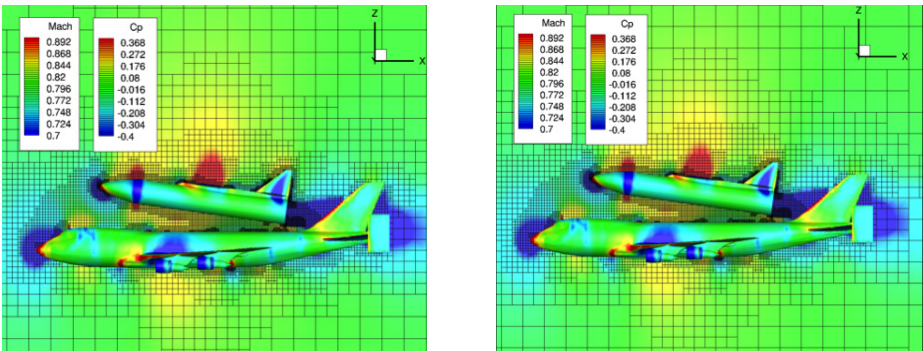


Figure 12(a). Mach number contours and surface pressures for the mated configuration ($M = 0.8$, $\alpha = 0^\circ$, $\theta = 8^\circ$ and $\Delta Z = 0$ ft).

Figure 12(b). Mach number contours and surface pressures for the mated configuration ($M = 0.6$, $\alpha = 0^\circ$, $\theta = 8^\circ$ and $\Delta Z = 0$ ft).

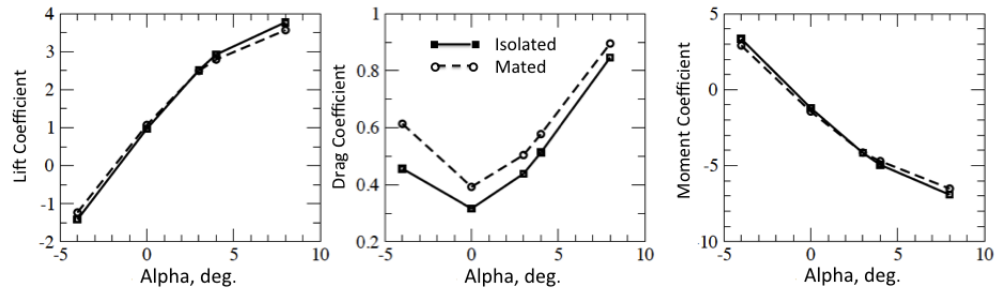


Figure 13. Interference effects on the SCA with respect to angle-of-attack at $M = 0.8$, $\theta = 2^\circ$.

A comparison between the isolated and mated aerodynamics is shown in Fig. 14 for the launch vehicle at $\theta = 2^\circ$. Here, the lift, drag, and pitching moment are affected substantially. The comparison shows that the launch vehicle experiences a lower lift in the mated configuration, and thus a lower drag as well. The effect is larger on the launch vehicle than on the SCA because a small area of the SCA is in the proximity of the launch vehicle, while nearly the entire launch vehicle experiences the effect of the SCA's presence. The same conclusion is valid when the launch vehicle is at $\theta = 5^\circ$.

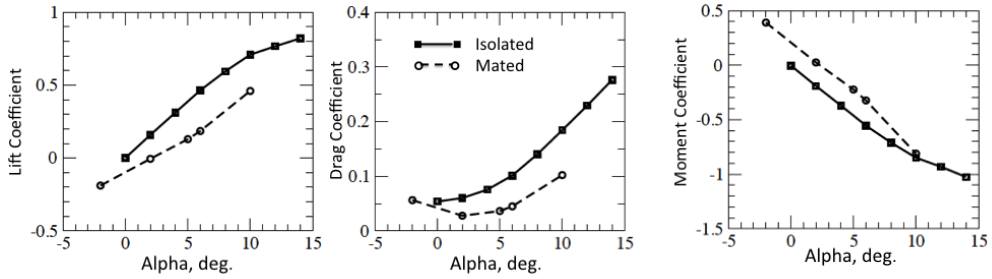


Figure 14. Interference effects on the launch vehicle with respect to angle-of-attack at $M = 0.8$, $\theta = 2^\circ$.

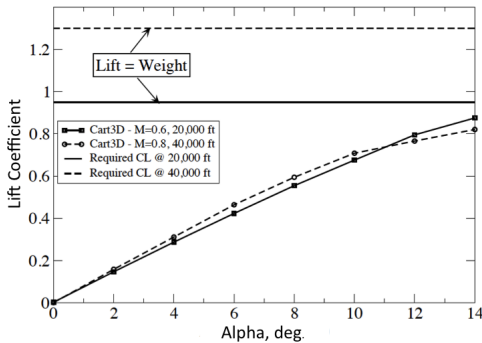


Figure 15. The lift generated in comparison to the weight of the isolated launch vehicle.

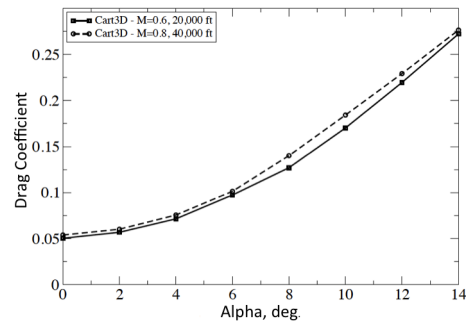


Figure 16. Comparison of isolated launch vehicle drag coefficients at Mach 0.6 and 0.8.

Figures 10-14 illustrate the advantages of CFD simulations during a conceptual design study. Flow physics insights, as depicted in Figs 10-12 are clearly infeasible with engineering methods. These methods cannot assess interference effects when the carrier and the launcher are mated together. These effects are quantified with CFD simulations as shown in Figs 13 and 14.

Figure 15 shows the lift coefficient of the launch vehicle as a function of the angle-of-attack to examine whether the stage separation can occur in level flight with the lift generated by the launcher wing. The lift generated by the chosen launch vehicle at both Mach 0.6 and 0.8 is not enough to achieve separation since the weight of the launch vehicle is more than the lift in each case. Thus, some pitching manoeuvre will need to be used in order to achieve proper stage separation. As seen in Figs 15 and 16, the aerodynamic coefficients on the isolated launch vehicle at Mach 0.6 are nearly the same as those at Mach 0.8.

The CFD results presented in this section thus far were for the launch vehicle with the 47ft payload fairing. The impact of shortening the payload fairing from 47ft to 30ft on the interference effects is shown in Fig. 17. For both vehicle lengths, the proximity effects affected both the mated aerodynamics and stage separation. However, the impact of the interference effect on stage separation is less for the shorter launch vehicle.

4.0 MATED SCA CRUISE PERFORMANCE

The first step in determining the launch capability of the SCA with the attached launch vehicle is to compute the steady-state cruise performance of the mated configuration. The pull-up manoeuvre for separation of the launch vehicle begins from this equilibrium flight condition. The cruise

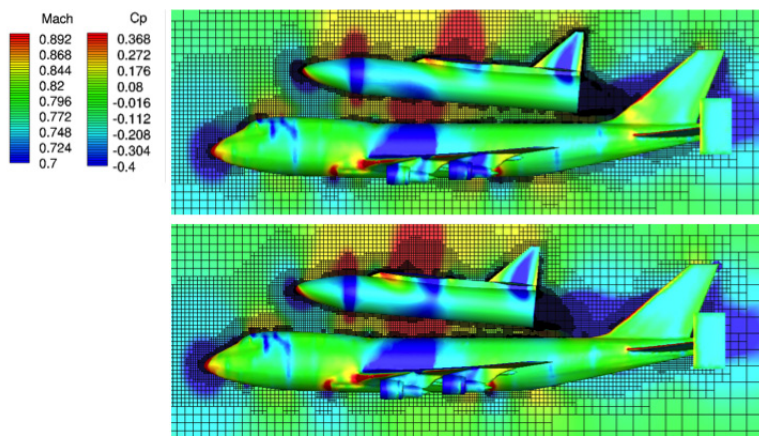


Figure 17. Effect of shortened payload fairing from 47ft (top figure) to 30ft (bottom figure) on the mated configuration aerodynamics (Cart3D simulations at Mach 0.8, $\alpha = 4^\circ$, $\theta = 5^\circ$, and $\Delta Z = 0$ ft).

performance of the mated SCA will be a function of the cruise Mach number, cruise altitude, and effective launch vehicle angle-of-incidence (wing incidence plus launcher incidence). The aerodynamic coefficients for the isolated launch vehicle at Mach 0.6 and Mach 0.8 were computed with the Cart3D software (Figs 15 and 16). The data were computed at Mach 0.7 with linear interpolation between the results for Mach numbers 0.6 and 0.8.

Recall that the wing incidence is at 0° in this study. Parametric variations of Mach number, cruise altitude, and launch vehicle incidence angle are conducted. At each combination, the equilibrium flight condition (total lift = total weight and total drag = thrust) is evaluated. Comparisons are then made to see if the total engine thrust of the SCA with JT9D-7J engines – each producing 50,000lbf of static thrust operating at maximum continuous power throughout the launching manoeuvre⁽¹⁶⁾ – is greater or equal to the total drag on the configuration at each flight condition.

Figure 18 presents the installed net thrust of the JT9D-7J turbofan engine at maximum continuous power rating as a function of Mach number and altitude. CFD lift coefficients for the SCA and experimental drag data for the B747-100^(33,34) are used.

In an equilibrium flight condition, the total lift of the mated configuration must equal the mated weight. At fixed altitude, flying at a Mach number corresponding to the maximum total mated lift-to-drag ratio results in the lowest total mated drag. The maximum lift-to-drag ratio for the mated configuration with or without interference aerodynamic effects occurs when the SCA is at roughly 3° angle-of-attack, independent of Mach number. Figure 19 shows that this ratio (with interference effects) has a value of approximately 14.5 at 2° effective launch vehicle incidence and is down to roughly 9.0 at 11° incidence.

Figure 20 presents the equilibrium total isolated drag as a function of launch vehicle effective incidence angle at Mach 0.6, 0.7, and 0.8 (solid lines) for a cruise altitude of 20,000ft. Figure 20(a) shows results without interference effects, and Fig. 20(b) shows results with interference effects. As the cruise Mach number is increased at fixed altitude, the free-stream dynamic pressure increases, resulting in a lower required equilibrium SCA angle-of-attack, which lowers induced drag. For all Mach numbers presented, the required SCA angle-of-attack is less than the angle-of-attack needed for maximum total lift-to-drag ratio, both with and without interference aerodynamics. The net result is increased total drag with increased cruise Mach number. As the incidence of the carried launch vehicle is increased, the total drag also increases due to higher launch vehicle drag.

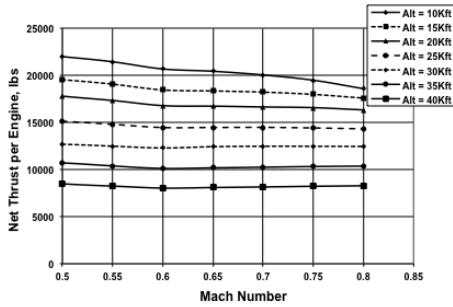


Figure 18. JT9D-7J net engine thrust at maximum continuous rated power.

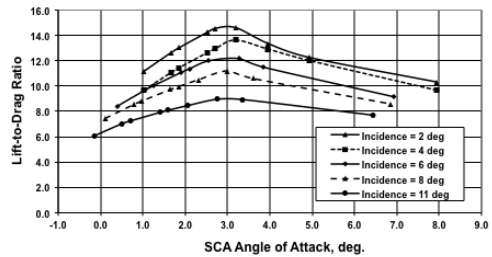


Figure 19. Mated lift-to-drag ratio with interference aerodynamics for various effective incidence of the launch vehicle.

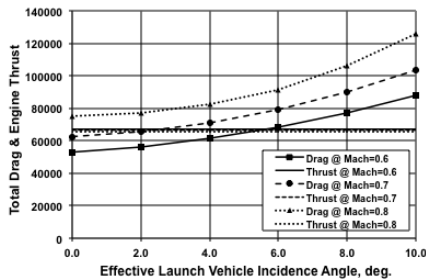


Figure 20(a). Total mated drag without interference effects and available engine thrust at 20,000ft altitude.

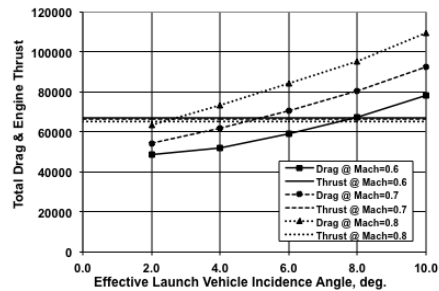


Figure 20(b). Total mated drag with interference effects and available engine thrust at 20,000ft altitude.

Figure 20 also shows the total net thrust available at maximum continuous power as a function of Mach number (dashed lines). The available net thrust of the JT9D-7J engine is almost independent of the flight Mach number at higher altitudes, due to higher ram drag with increasing Mach number being offset by higher cycle pressure ratio. The intersection of the total drag and the total net thrust available represents an equilibrium flight condition for the mated configuration.

As shown in Fig. 20(a), when total mated aerodynamics are considered without interference effects, the launch vehicle could be carried at Mach 0.6 and an effective incidence angle of up to approximately 5.5°. At Mach 0.7, the maximum useful incidence angle decreases to roughly 2.5°. No flight equilibrium point is found for the Mach 0.8 case, for which total drag is always greater than available net thrust. As shown in Fig. 20(b), when total mated aerodynamics are considered with interference effects, the launch vehicle could be carried at incidence angles of up to approximately 7.5° at Mach 0.6, roughly 4.75° at Mach 0.7, and barely 2° at Mach 0.8. This increase in allowable launch vehicle effective incidence angle is due to lower total system drag when interference effects are considered.

Figure 21 shows the mated drag and engine thrust for a cruise altitude of 25,000ft both without interference effects (Fig. 21(a)) and with interference effects (Fig. 21(b)). At low effective launch vehicle incidence angles and Mach 0.6, the SCA angle-of-attack required increases to a value above the angle-of-attack necessary to achieve maximum mated lift-to-drag (L/D) ratio for cases both with and without interference effects. This is because the dynamic pressure is relatively low (approximately 200psf) at this flight condition. This means that the configuration is flying on the

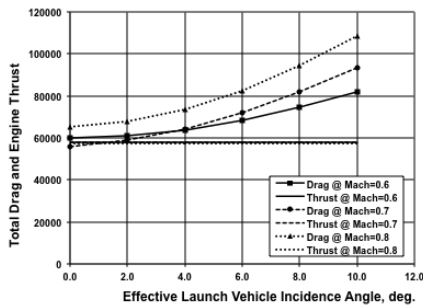


Figure 21(a). Total mated drag without interference effects and available engine thrust at 25,000ft altitude.

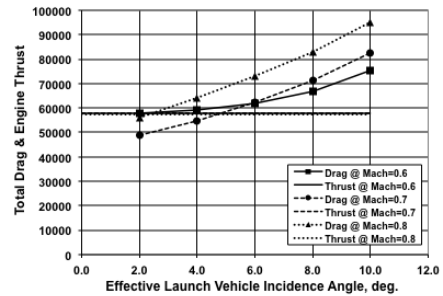


Figure 21(b). Total mated drag with interference effects and available engine thrust at 25,000ft altitude.

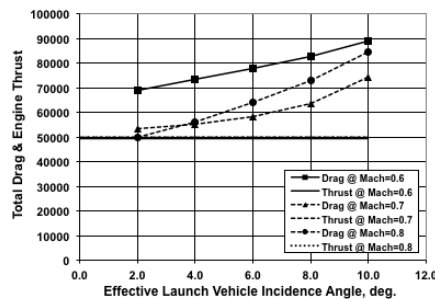


Figure 22. Total mated drag with interference effects and available engine thrust at 30,000ft altitude.

backside of the power curve. Increasing the Mach number to 0.7 increases the dynamic pressure (approximately 270psf). At this Mach number, the SCA angle-of-attack required is very close to the mated maximum L/D ratio. The net result is lower total drag with or without interference effects at Mach 0.7 compared to Mach 0.6. At low effective launch vehicle incidence, that drag is less than or equal to the available thrust. As the Mach number is further increased to Mach 0.8, the required SCA angle-of-attack is less than the maximum L/D value. The net result is a total drag greater than the available thrust.

For total mated drag without interference effects (Fig. 21(a)), the maximum launch vehicle incidence angle is just below 1.5° at Mach 0.7, and again no solutions are found for the Mach 0.8 case. However, when total mated drag is considered with interference effects (Fig. 21(b)), the maximum launch vehicle effective incidence angle is 2° at Mach 0.6, just below 4.75° at Mach 0.7 and 2° at Mach 0.8.

Finally, Fig. 22 shows the total mated drag with interference effects and engine thrust available at 30,000ft altitude. The high induced drag at Mach 0.6 results in drag levels above both Mach 0.7 and 0.8. The available engine thrust is less than the equilibrium total mated drag with interference effects for all Mach numbers investigated at this altitude. The same conclusion is valid when considering the total mated drag without interference effects.

Engineering-based aerodynamic methods are questionable for developing a credible conceptual mated configuration design. Because the SCA cruise performance requires mated aerodynamics with interference effects, CFD aerodynamic analysis is essential.

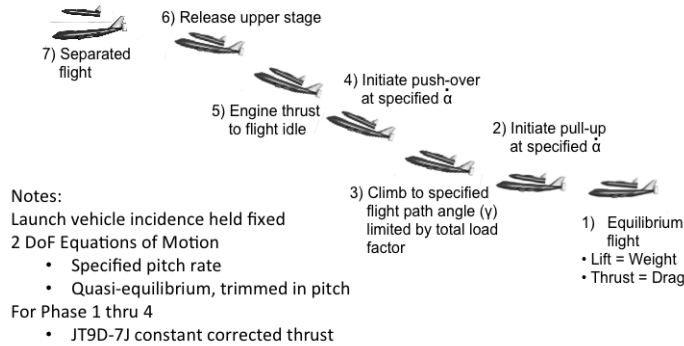


Figure 23. Separation sequence.

As a result of this mated cruise performance investigation, we focus our study on a launch manoeuvre executed at 20,000ft cruise altitude and Mach 0.6, giving the largest range of possible launch vehicle incidence angles. The feasibility of cruising at a 20,000ft altitude could depend on the choice of the launch vehicle. The chosen cruise Mach number is consistent with the SCA Mach limit⁽¹⁶⁾.

The performance of the SCA is limited. The airspeed is limited to Mach 0.6 with and without an orbiter, and the typical cruising altitudes are 13,000-15,000ft with the Orbiter and 24,000-26,000ft without the orbiter⁽¹⁶⁾. The HLS chose to conduct stage separation at Mach 0.7 and 25,000ft altitude.

5.0 ENGINEERING SEPARATION ANALYSIS

An engineering-based analysis was conducted to assess what flight conditions would enable the launch vehicle to undergo positive separation from the SCA. Factors impacting launch vehicle separation include free-stream dynamic pressure, SCA angle-of-attack, launch vehicle incidence, flight path angle, pitch rates, and the support strut configuration. The analysis approach taken in this study was to formulate a simplified engineering separation dynamics model, and then examine parametric combinations of the aforementioned variables to define a feasible design space of positive separation conditions. No trajectory optimisation was conducted. This section presents results from one set of parameter combinations, with aerodynamic interaction effects on the launcher considered.

The separation event sequence is presented in Fig. 23, proceeding in time from right to left. The separation process begins with the 1g equilibrium flight condition. The thrust limits of the JT9D-7J turbofan were not imposed in this analysis, so not all of the initial flight conditions are necessarily achievable with the SCA. During the separation sequence, the launch vehicle incidence angle is held fixed. From the equilibrium flight condition, the separation sequence is initiated by a pitch-up manoeuvre at a specified rate of change of the SCA angle-of-attack, $d\alpha/dt$.

The pull-up of the mated configuration is continued until a specified flight path angle is achieved, limited by an allowable normal load factor. Once the desired flight path angle is established, a pitch-over manoeuvre is initiated, again at a specified $d\alpha/dt$. At that time, the engine is throttled down at a specified rate to the flight idle power setting. The mated configuration continues in the pitch-down manoeuvre until launch vehicle separation conditions are reached, whereupon the launch vehicle is released and the separated flight phase begins. The flight path is assumed to occur in a vertical plane, resulting in two-degrees-of-freedom (2-DOF) equations of motion, which are

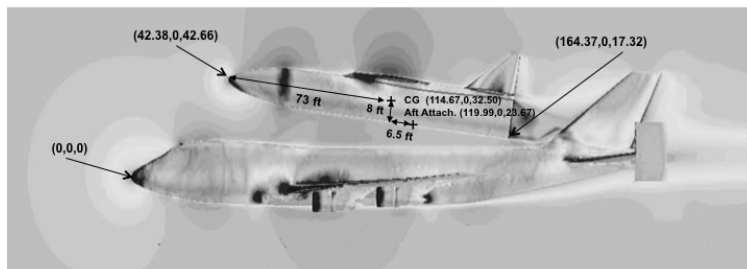
(a) $\alpha = 0^\circ$ and $\theta = 5^\circ$ (b) $\alpha = 0^\circ$ and $\theta = 8^\circ$

Figure 24. Co-ordinates of key locations of the launcher with respect to the nose of the SCA.

solved with specified pitch rates under quasi-equilibrium and trimmed in pitch conditions. Prior to the engine spool-down phase, the JT9D-7J is assumed to operate at constant corrected thrust.

Figure 24 shows the locations of the launcher relative to the SCA when the launcher is at 5° and 8° incidence. The X and Y co-ordinates of the launcher's and SCA's centres of gravity are the same relative to the co-ordinates of the nose of the SCA.

Figure 25(a) presents the simplified engineering model for the launch vehicle attachment strut arrangement. The arrangement consists of a forward and an aft strut member, with a drag link attachment for the aft strut. The struts are assumed to attach to the launch vehicle using a ball joint, with pinned joints on the SCA side. The forward strut reacts only to normal loads, either in compression or tension, while the aft strut reacts to both normal and axial loads through the drag link. The assumed attachment strut arrangement is a statically determinate structure and, given the acceleration and aerodynamic loads on the vehicles, the strut normal and axial forces can be resolved.

Starting from the equilibrium phase, the 2-DOF equations of motion for the mated configuration are integrated using a simple, first-order Euler method. Pitch-up and pitch-down rates are specified. After each integration time step (0.1 seconds), the forces acting on the launch vehicle are computed to see if the positive separation criterion is met.

Figure 25(b) shows the free-body diagram for the launch vehicle in mated flight, and denotes the forces and moments acting on the launch vehicle, including the reaction forces from the SCA through the support strut system.

The velocity of the launch vehicle, V , is computed from the mated configuration's velocity at the centre of gravity (V_{CG}) and the rotational velocity of the launch vehicle about the system centre of

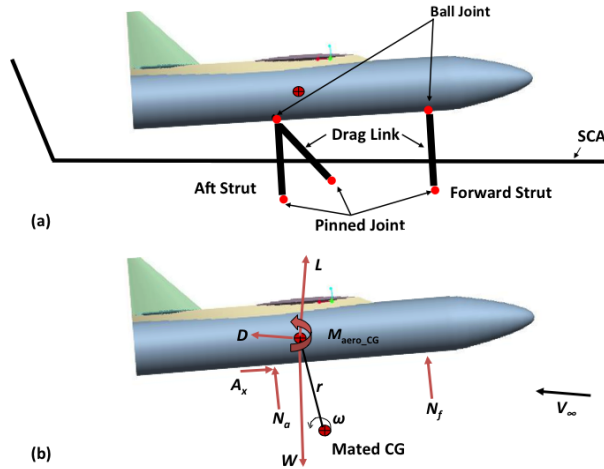


Figure 25. (a) Launch vehicle attachment strut arrangement and (b) launch vehicle mated flight free-body diagram.

gravity (Equation (1)). For the rotation rates considered here, the induced velocity is small and is neglected, and the resulting aerodynamic forces are all evaluated at the system free-stream velocity. The equation of motion of the launch vehicle is shown in Equation (2). The time derivative of the centre-of-mass velocity, \dot{a} , is known at this point. Along with the aerodynamic forces acting on the launch vehicle and its weight, Equation (2) can be resolved into wind or body axis in the vertical plane, resulting in two independent equations. Aerodynamic forces are evaluated at the centre of gravity (CG). Finally, the moments on the launch vehicle are evaluated about the aft strut attachment point (Equation (3)), where the aerodynamic moment about the CG (M_{aero_CG}) has been translated to the aft support point (M_{aero_Aft}). This system of three equations is solved for the unknowns: two normal forces N_f and N_a , and the axial force A_x . When both the normal forces are in tension, the separation condition is reached.

$$\mathbf{V} = \mathbf{V}_{CG} + \boldsymbol{\omega} \times \mathbf{r} \approx \mathbf{V}_{CG} \quad \dots (1)$$

$$m\dot{\mathbf{a}} = m(\dot{\mathbf{a}}_{CG} - \omega^2 \mathbf{r}) = \mathbf{L} + \mathbf{D} + \mathbf{W} + \mathbf{N}_f + \mathbf{N}_a + \mathbf{A}_x \quad \dots (2)$$

$$\sum M_{Aft} = M_{W_Aft} + M_{aero_Aft} + M_{Nf_Aft} = 0 \quad \dots (3)$$

The aerodynamic characteristics needed for this engineering analysis were computed for the launch vehicle in the mated configuration using Cart3D, as presented in the preceding sections. These results are summarised for Mach 0.8 in Figs 26 through 28 as a function of SCA angle-of-attack and the launch vehicle incidence angle. Similar results are expected at Mach 0.6, since the aerodynamic coefficients for the isolated launch vehicle at Mach 0.6 and Mach 0.8 are nearly the same (Figs 15 and 16). The data were computed at Mach numbers of 0.6 and 0.8, with linear interpolation for other Mach numbers. As the incidence angle of the launch vehicle is increased, the launch vehicle lift, drag, and pitching moment coefficient generally all increase across the range of the SCA angle-of-attack.

As mentioned above, eight different parameters were investigated, including cruise Mach number and altitude, launch vehicle incidence, pull-up flight path angle, pitch-up and pitch-down rate,

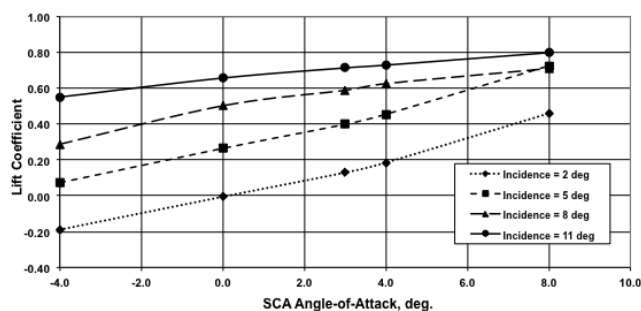


Figure 26. Launch vehicle lift coefficient versus SCA angle-of-attack and launch vehicle incidence angle, Mach number = 0.8 and reference surface area = 1,063ft².

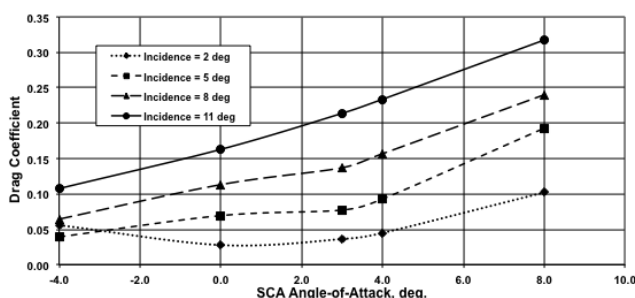


Figure 27. Launch vehicle drag coefficient versus SCA angle-of-attack, Mach number = 0.8 and reference surface area = 1,063ft².

allowable normal load factor, and aft strut location relative to the launch vehicle CG. Only one case will be presented here, and comparison of the various trajectory parameters will be presented for the isolated aerodynamics and the mated aerodynamics. The flight parameters for the presented case are: Mach 0.6 at 20,000ft altitude, launch vehicle incidence angle of 8°, pull-up flight path angle of 3°, limit normal load factor of 1.15, pitch-up and pitch-over rates of +2° and -2° per second respectively, and an aft strut location of 5% of the body length behind the launch vehicle CG location. The Cart3D aerodynamics data are for the 47ft payload fairing.

Figure 29 presents the time history of the SCA angle-of-attack for the selected case, comparing isolated and mated aerodynamics. The SCA angle-of-attack starts from the equilibrium value and increases at the commanded pitch rate until the normal load factor limit is reached. The mated configuration continues to climb to the specified flight path angle of 3°, and then the pushover manoeuvre is initiated. The SCA angle-of-attack required for the mated aerodynamics is higher compared to the isolated aerodynamics, reflecting the loss of launch vehicle lift coefficient in the mated configuration. Also, the mated aerodynamics results in a slightly longer captured flight phase, on the order of only 0.25 seconds.

Figure 30 presents the time history of the required total engine thrust, with the mated aerodynamics requiring less thrust due to the lower drag on the launch vehicle in the mated configuration. For reference, the available thrust of the four JT9D-7J engines at maximum continuous power setting is also plotted, indicating marginal performance of the SCA for this flight condition.

The free-stream dynamic pressure history is presented in Fig. 31. As the pull-up manoeuvre is executed, there is a bleed-off in the dynamic pressure for both the isolated and mated aerodynamic

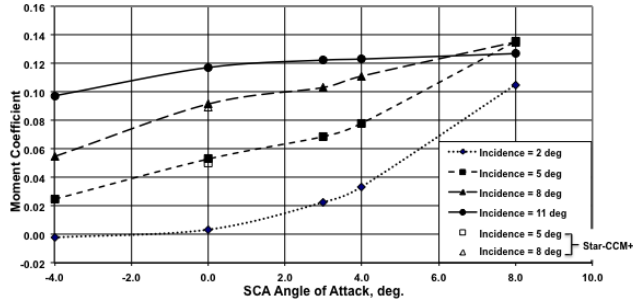


Figure 28. Launch vehicle pitching moment coefficient at aft strut versus SCA angle-of-attack, Mach number = 0.8 and reference surface area = 1,063ft², l_{ref} = 60.732ft.

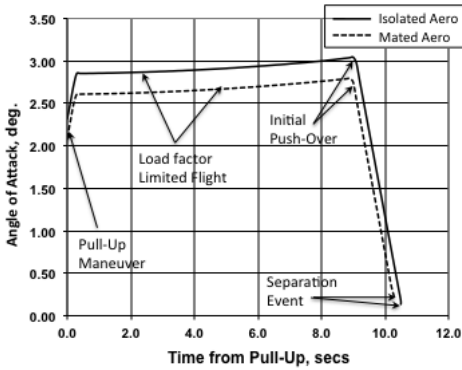


Figure 29. SCA angle-of-attack versus time from pull-up.

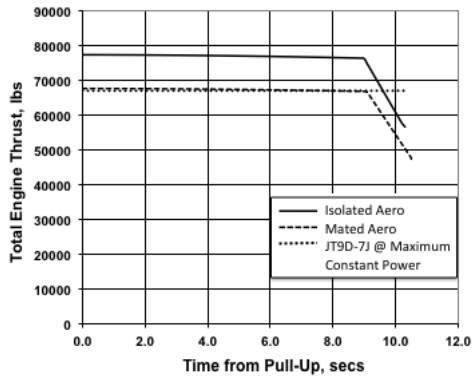


Figure 30. SCA total engine thrust versus time from pull-up.

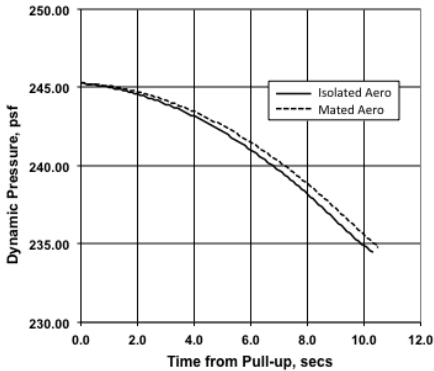


Figure 31. Free-stream dynamic pressure versus time from pull-up.

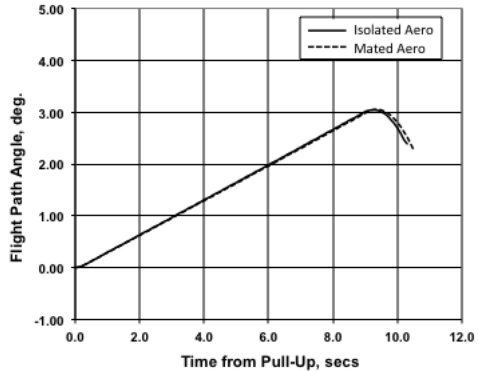


Figure 32. Flight path angle versus time from pull-up.

models, but on the order of only 5%. Altitude gain before separation is only on the order of approximately 250ft.

Figure 32 shows the flight path angle time history, which is again very similar for the isolated and mated aerodynamic models. The staging condition for the isolated aerodynamics is at a flight path angle of 2.55°, while for the mated aerodynamics it is 2.39°.

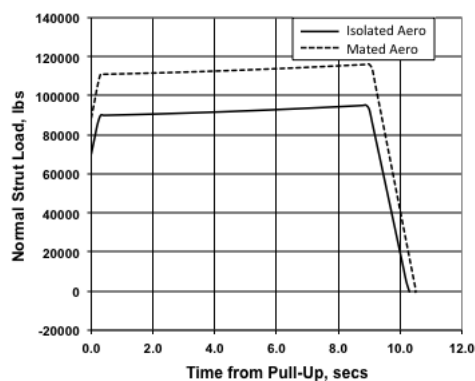


Figure 33. Aft strut normal load versus time from pull-up.

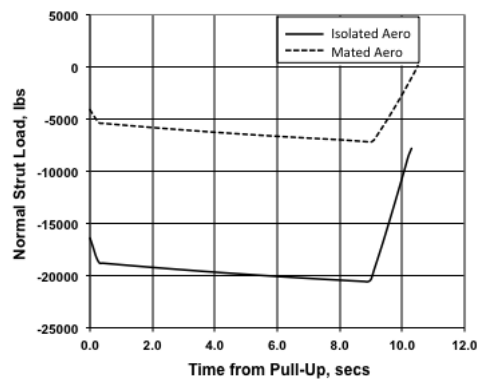


Figure 34. Forward strut normal load versus time from pull-up.

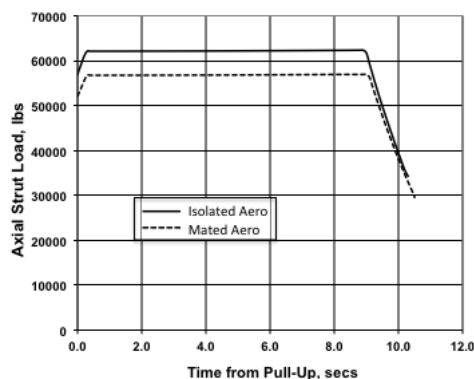


Figure 35. Aft strut axial load versus time from pull-up.

Time histories of the strut forces during the separation manoeuvre are presented in Figs 33 through 35. After the pull-up manoeuvre is initiated, the more normal compressive load is transferred to the aft strut. The aft strut normal load is higher for the mated aero model, due to the loss of launch vehicle lift in the mated configuration, resulting in more downward load on the aft strut compared to the isolated case. With the launch vehicle incidence angle set at 8° , the forward strut is already in tension for both mated and isolated aerodynamic models. Separation occurs at roughly 10.5 seconds after pull-up initiation for both, again with the mated case taking only slightly longer. Finally, Fig. 35 shows that the aft strut axial load (roughly equal to the drag of the launch vehicle) is lower for the mated aero model, due to lower predicted drag in the mated configuration.

There is a general reduction in both the lift and drag coefficient for the launch vehicle in the mated configuration, with a slight reduction in the pitching moment coefficient. These differences lead to fairly different values in the support strut reaction loads. Accurate assessment of the mated aerodynamic parameters is required to resolve the strut loads for preliminary design purposes.

When carrying the space shuttle orbiter, the SCA has limited capability in terms of cruise Mach number and altitude, and is generally limited to altitudes of 20,000ft or less at Mach 0.6⁽¹⁶⁾. For 1g level flight at Mach 0.6 and 20,000ft altitude, the launch vehicle incidence must be less than or equal to 7.5° .

In general, the location of the aft support strut needs to be fairly close to the launch vehicle's centre of gravity – on the order of 5% of the vehicle body length. As the aft strut attachment approaches the CG, the moment generated by the launch vehicle weight is reduced, allowing for nose-up aerodynamic rotation of the launch vehicle about the aft strut attachment point.

For positive separation, the launch vehicle incidence angles needs to be 7° or higher. Of all the cases examined, no 5° launch vehicle incidence cases had safe separation, and a limited number of 6° cases were successful at the lowest Mach (0.6) and altitude (20,000ft) combination. The SCA angle-of-attack at separation conditions ranges from approximately -0.5° to $+1.0^\circ$. As staging Mach and altitude increase, the minimum required launch vehicle incidence angle also increases, resulting in generally higher required engine thrust. However, all successful separation cases exceeded the JT9D-7J maximum continuous power setting. This suggests that a screw-jack arrangement for the forward strut would be needed for the SCA/selected launch vehicle configuration, in order for the launch vehicle to be carried to the required flight condition at zero or low incidence angle. As the pull-up manoeuvre is initiated, the launch vehicle incidence angle is increased by extension of the forward support strut. As the staging Mach and altitude are increased, maximum obtainable separation flight path angle decreases.

In summary, the engineering-based separation analysis was conducted for the SCA/launch vehicle configuration both with and without aerodynamic interference effects for a range of flight trajectory and support strut arrangements. No configuration or separation trajectory optimisation was attempted. Eight different parameters were investigated, resulting in approximately 3,000 cases – a very limited number of cases.

For the cases examined, interference aerodynamic effects resulted in slightly longer mated flight mode, with a marginally reduced flight path angle at separation. Higher pitch-over rates mitigate this trend somewhat. The Mach number, altitude, and free-stream dynamic pressure are very similar to the isolated aero results. The support strut reaction loads are, in general, very different for the isolated versus mated aerodynamics, with lower axial load but higher compressive loads on the aft strut.

6.0 TRAJECTORY

To evaluate whether the stage separation manoeuvre will be successful and avoid recontact, the trajectory of each stage must be determined. The intended use of trajectory results determines what level of fidelity is required for the trajectory analysis tools. The trajectory analytical fidelity varies from Level 0 to Level 4, as described in Table 6. In the present concept assessment study, Fidelity Level 1 methods were used to determine trajectories of the carrier and the launcher after staging. The HLS also used Level 1 methods⁽¹⁵⁾. Note that Level 3 and Level 4 are, respectively, necessary for preliminary design and final design efforts.

To determine the success of staging, trajectories of the SCA and the launch vehicle after separation were simulated in Programme to Optimise Simulated Trajectories II (POST2), using the 3-DOF option with 2-DOF input data. Both isolated and interference aerodynamic databases were simulated. Since the relative positions of the two vehicles are the most important factors needed to determine if there is re-contact, the trajectories of both vehicles were simulated simultaneously in POST2. The CFD lift polar for the SCA and experimental drag data for the B747-100^(33,34) used for this analysis were based on isolated aerodynamics. The study of the interference effects between the SCA and the launcher used the Cart3D-generated data.

At separation ($t = 0$), the SCA weighs 470,000lbm. It immediately pitches down at -2° per second until $\alpha = -2^\circ$. The SCA then maintains $\alpha = -2^\circ$ and continues its descent until the flight

Table 6**Fidelity levels for trajectory, guidance, navigation and control (adapted from Ref. 15)****Fidelity Description****level**

0	Rocket equation or energy methods; path-following simulation.
1	Optimised ascent, flyback, and reentry 3-DOF point mass simulation; untrimmed.
2	Optimised ascent, flyback, and reentry 3-DOF (pitch trim) point mass simulation; longitudinal stability and control evaluation.
3	Optimised ascent, flyback, and reentry 6-DOF simulation; longitudinal, lateral, and yaw stability and control evaluation; perfect guidance, navigation, and control.
4	Optimised ascent, flyback, and reentry 6-DOF simulation; longitudinal, lateral, and yaw stability and control evaluation; real guidance, navigation, and control with gain scheduling or similar lags, noise, etc.

Table 7**Flight conditions at separation**

	Without interference	With interference
Altitude, ft	20,168	20,170
Flight path angle, deg	2.72	2.68
Velocity, ft/s	609.7	609.7
Mach no.	0.588	0.588
SCA alpha, deg	0.128	0.118
Launch vehicle alpha, deg	8.128	8.118
Dynamic pressure, psf	234.125	234.109

path angle is -15° . It then pitches up at 2° per second until the flight path angle is 0° , and then continues with equilibrium level flight (lift = weight, thrust = drag).

The launch vehicle weighs 240,000lbm at the separation. This study assumes that the SCA is equipped with a screw-jack arrangement. Just before separation, this system sets the pitch attitude of the launch vehicle to 8° relative to the SCA. From this position after separation, the launch vehicle pitches up at 2° per second until the angle-of-attack is 14° , then holds this angle. The launch vehicle engine is powered by a liquid oxygen (LOX)/hydrogen rocket with a vacuum thrust of 540,000lbf and specific impulse (Isp) of 440 seconds. The following section will look at the trajectories for three cases: (1) when the launch vehicle engine stays off, (2) when the engine turns on at a vertical separation distance of 500 ft, and (3) when the engine turns on at a vertical separation distance of 1,000ft. Launch vehicle trajectories are presented with and without the proximity interference effects.

As mentioned in the previous section, there is a reduction in lift, drag, and pitching moment due to the aerodynamic interference. Table 7 shows the flight conditions at separation, both with and without the interference effects. The differences are small.

Figures 36(a) and 36(b) show the lift and drag coefficients of the launch vehicle at 8° incidence, as functions of the vertical separation distance. When the vertical separation of the two vehicles is greater than 400ft, the interference effect is assumed to vanish. The 'as modeled' aerodynamic coefficients are plotted in these figures using computed values for the forces experienced by the

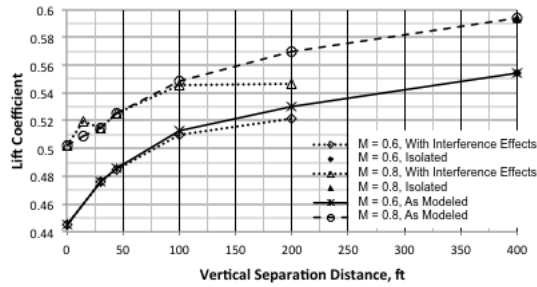


Figure 36(a). Launch vehicle interference lift coefficient.

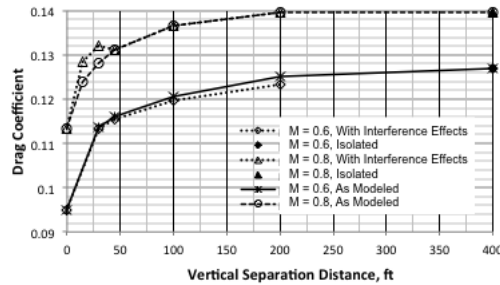


Figure 36(b). Launch vehicle interference drag coefficient.

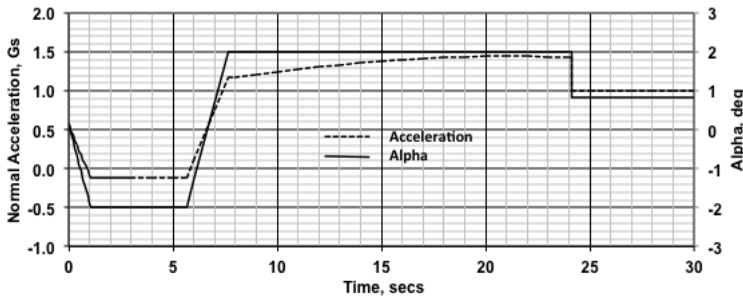


Figure 37. SCA normal acceleration and angle-of-attack with staging, at Mach 0.6, 20,000ft altitude, and 2.72° flight path angle.

isolated launch vehicle at 400ft vertical separation, and using the known forces acting on it in proximity of the SCA. No relative change in x -direction was considered. At Mach 0.6, the isolated (assumed separation distance, ΔZ , is 400ft) lift coefficient (CL) and drag coefficient (CD) are 24.7% and 30.5% more than the mated (separation distance, ΔZ , is 0ft) CL and CD , respectively.

Figure 37 shows the SCA normal load and angle-of-attack as a function of time after staging. The maximum value remains below 1.5g and above the negative g limit – well under the design limit of the SCA.

Figure 38(a) shows the trajectories of the SCA and the unpowered launch vehicle. The SCA dives from 20,170ft to 17,700ft and then levels off. Unpowered launch vehicle trajectories with and without interference effects are nearly the same. Figure 38(b) shows the vertical separations between the SCA and the launch vehicle. Notice that the interference effects go away after six seconds because the vertical separation is greater than 400ft. The interference effects cause the

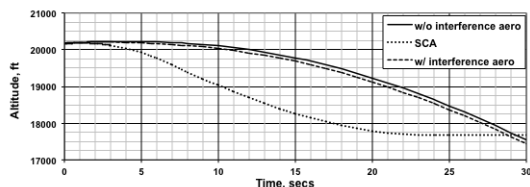


Figure 38(a). Time histories of altitude with launch vehicle staging at Mach 0.6, 20,000 ft altitude,

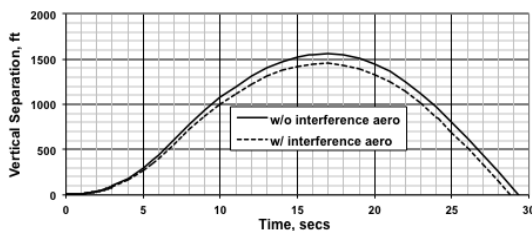


Figure 38(b). Time histories of the vertical separation between vehicles, with launch vehicle engine off.

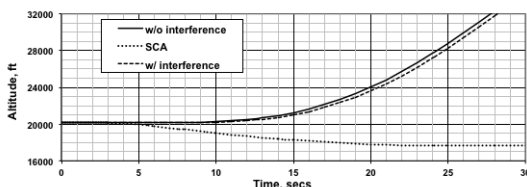


Figure 39(a). Launch vehicle trajectories after separation, with launch vehicle engine activated at 500 ft vertical separation.

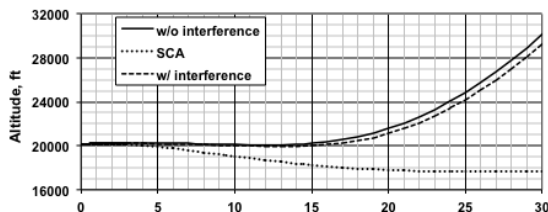


Figure 39(b). Launch vehicle trajectories after separation, with launcher engine activated at 1,000 ft vertical separation.

launch vehicle a slight, 0.36% loss of altitude at ten seconds after separation. At ~19 seconds, the pitch attitude of the launch vehicle becomes negative. Activating the engine after this time would cause a downward component of the thrust vector.

Figure 39 shows the SCA trajectory and the powered launch vehicle trajectories with and without the interference effects. The launch vehicle engine is activated at 500 ft (Fig. 39(a)) and at 1,000 ft (Fig. 39(b)) vertical separation. The interference effect causes 2-3% loss in altitude at 25 seconds.

Table 8 summarises the vertical separation of the two vehicles at 400, 500, 1,000, and 1,500 ft with the rocket engine off. Notice that the vertical separation is always less than 1,500 ft with interference effects.

Figure 40 shows the relative positions of the SCA and the powered launch vehicle as a function of down-range distance, with the engine activated at 500 ft vertical separation (at 6.6 seconds) and

Table 8
Vertical separation distance with launch vehicle engine off

	400ft	500ft	1,000ft	1,500ft
Time (sec), without interference	5.706	6.336	9.450	14.52
Time (sec), with interference	5.958	6.601	9.968	N/A
Δ Time	0.253	0.265	0.518	N/A

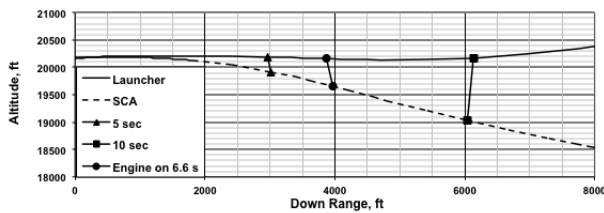


Figure 40. Relative positions of the SCA and launcher for staging at Mach 0.6, 20,000ft altitude and with engine on at 500ft ΔZ .

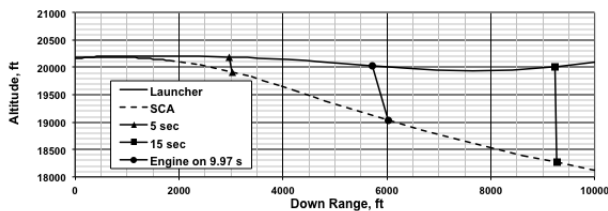


Figure 41. Relative positions of the SCA and launch vehicle for staging at Mach 0.6, 20,000ft altitude, and with engine on at 1,000ft ΔZ .

with interference effects included. The relative down-range (horizontal) distance is indicated at three event times: 5, 6.6, and 10 seconds after separation. At the engine activation time, the launch vehicle is 105.2ft behind the SCA. It overtakes the SCA at 9.26 seconds, when it is ~5,500ft down range with a vertical separation distance of 986ft. How the plume shock from the launch vehicle engine affects the SCA is not within the scope of this study, but it is a concern.

Figure 41 is similar to Fig. 40. In this case, the launch vehicle engine is started when the vertical separation is equal to 1,000ft (9.97 seconds after separation). At this point, the launch vehicle is 306ft behind the SCA. It overtakes the SCA at 15.2 seconds, with a vertical separation distant of ~1,800ft. This is probably a safer scenario than when the engine is turned on at 500ft vertical separation.

Figure 42 shows the relative distances from the SCA CG to both the highest forward point of the SCA tail and the lowest aft point of the launcher. Figure 43 shows the relative distance between the latter two locations. During the initial staging period, there is no contact between these two points. The interference effects are considered.

In summary, the launch vehicle will fail to commence a climbing flight after staging unless its engine is started while its pitch attitude is still positive, which is within ~19sec after separation. Aerodynamic interference effects are observed during mated flight and during staging, including during the pull-up manoeuvre, load factor limited flight, push-over manoeuvre, separation event, and the first few seconds (~6sec) after separation. Safety issues may prevent the start of the launch vehicle engine within 5 or 10sec after staging.

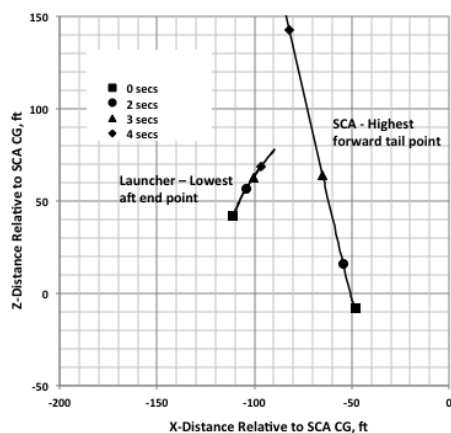


Figure 42. Relative distances between the SCA centre of gravity and the SCA highest forward tail tip and the launcher lowest aft end, after staging at Mach 0.6 and 20,000ft altitude.

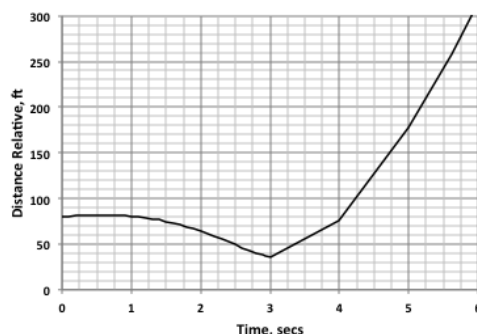


Figure 43. Relative distance between SCA highest forward tail tip and launcher lowest aft end, after staging.

7.0 CONCLUSIONS AND PERSPECTIVES

Assessment of the credibility of a TSTO stage separation concept from a widebody subsonic carrier aircraft principally requires accurate analysis of aerodynamics (forces and, particularly, moments) during staging to account for interference effects from the proximities of the two large vehicles. These aerodynamic effects determine whether safe mated flight and stage separation are feasible. The capability of engineering-based aerodynamic methods to properly quantify aerodynamic interference effects and to develop credible conceptual designs for mated configurations is questionable. The credibility of conceptual designs can be established with a combination of engineering methods, CFD simulations, and trajectory analysis.

Currently, a few designers routinely use CFD for conceptual point designs. All designers use both CFD and test data from ground-based test facilities to develop preliminary designs. The Fidelity Level 0 and 1 aerodynamic approaches for conceptual designs could be eliminated, because CFD and supercomputing capabilities have advanced sufficiently to provide fast and credible simulations for assessing conceptual designs.

As staging Mach and altitude increase, the minimum required launch vehicle incidence increases (with the vehicle's wing remaining at the same incidence). Higher incidence angles result in increased engine thrust levels required to propel the mated configuration. With increasing staging Mach and altitude, the maximum obtainable separation flight path angle decreases. Safety concerns determine how far away the launch vehicle needs to be from the carrier aircraft before starting the launch vehicle engines.

For the SCA carrier vehicle, the interference aerodynamics have a modest impact on the separation conditions and separated flight trajectories, but have a significant impact on the interaction forces. The loads from these interaction forces affect the design of the attachment struts that mate the launch vehicle with the carrier aircraft.

The incidence of the launch vehicle plus its wing incidence (i.e., the effective incidence of the launcher) needs to be 7° or higher to stage from the SCA at Mach 0.6 and 20,000ft altitude. The launcher's effective incidence angle can go only to approximately 7.5° . With flight Mach numbers varying from 0.6 to 0.8 and altitudes varying from 20,000 to 30,000ft, no 5° effective

incidence cases and limited 6° cases were found to separate successfully. The SCA angle-of-attack at separation ranges approximately from -0.5° to $+1.0^\circ$. Since the SCA is operationally limited to Mach 0.6, staging at higher Mach numbers is not feasible. Widebody aircraft, such as the An-225 and B747-800F, could launch at Mach numbers greater than 0.6.

Operational subsonic widebody aircraft or a new subsonic aircraft with two fuselages could be used for staging of a launch vehicle to place a medium-weight payload in LEO. New aircraft with a single fuselage could be developed for staging at supersonic and hypersonic Mach numbers. Stage separation is a critical design issue for all TSTO system concepts with air-breathing carrier aircraft.

ACKNOWLEDGEMENT

Lorien F. Wheeler and Jill Dunbar, Computer Sciences Corporation, edited the manuscript of this paper.

REFERENCES

1. AUGENSTEIN, B.W., HARRIS, E.D. with AROESTY, J., BLUMENTHAL, L., BROOKS, N., FRELINGER, D., GARBER, T., GOTTENMOELLER, R., HILAND, J., LIU, S.K., PACE, S., ROSEN, J., ROWELL, L. and STUCKER, J. The National Aerospace Plane (NASP): Development issues for the follow-on vehicle, Executive Summary, 1993, RAND, R3878/1-AF, Santa Monica, CA, USA.
2. HALLION, R.P. and YOUNG, J.O. *Space Shuttle: Fulfillment of a Dream, The Hypersonic Revolution, Vol 2*, 1987 HALLION, R.P. (Ed), Special Staff Office, Aeronautical Systems Div, Wright-Patterson AFB, OH, USA.
3. HALLION, R.P. Hypersonic power projection, 2010, Mitchell Paper 6, Mitchell Institute for Airpower Studies.
4. ASHFORD, D.M. New commercial opportunities in space, *Aeronaut J*, February 2007, pp 61-75.
5. Loss of M-21 and D-21 On 30 July 1966, http://www.wvi.com/~sr71webmaster/M21_Crash.htm.
6. Shuttle Enterprise free flight, <http://grin.hq.nasa.gov/ABSTRACTS/GPN-2000-000218.html>.
7. <http://www.buran.ru/htm/molniya.htm>.
8. HANNIGAN, R.J. *Spaceflight in the Era of Aero-Space Planes*, 1994, Krieger Publishing Co, p 112.
9. National Aero-Space Plane, Restructuring Future Research and Development Efforts, 1993, Rept NSIAD-93-71, US Government Accounting Office.
10. RICH, B.R. and JANOS, L. *SkunkWorks: A Personal Memoir of My Years at Lockheed*, 1994, Little Brown and Co, Boston, MA, USA.
11. <http://www.reactionengines.co.uk/sabre.html>
12. Access to space, Advance Technology Team final report, Volume 1, Executive Summary, July 1993, NASA.
13. <http://www.scaled.com/>
14. ALLEN, P.G. Announces revolution in space transportation, Stratolaunch Press Release, Stratolaunch Systems, 13 December 2011, <http://www.stratolaunch.com>.
15. Horizontal launch: A versatile concept for assured space access, Report of the NASA-DARPA Horizontal Launch Study, NASA SP 2011-215994.
16. Shuttle carrier aircraft, Fact Sheets 8 December 2009, NASA Dryden Flight Research Center, <http://www.nasa.gov/centers/dryden/news/FactSheets/FS-013-DFRC.html>.
17. WILLIAMS, J. and VUKELICH, S. The USAF stability and control digital DATCOM, AFRL-TR-79-3032 USAF DATCOM User's Manual, 1978.
18. http://www.wikipedia.org/wiki/United_States_Air_Force_Stability_and_Control_Digital_DATCOM.
19. MELTON J.E., BERGER, M.J. and AFTOSMIS, M.J. 3D Applications of a cartesian grid Euler method, July 1993, AIAA Paper 95-0853-CP.
20. AFTOSMIS, M.J., BERGER, M.J., and ADOMOVICIUS, G. A parallel multilevel method for adaptively refined cartesian grids with embedded boundaries, January 2000, AIAA Paper 2000-0808.
21. VAN LEER, B., TAI, C-H., and POWELL, K.G. Design of optimally smoothing multi-stage schemes for the Euler equations, AIAA Paper 89-1933.

22. AFTOSMIS, M J., BERGER, M.J. and MELTON, J.E. Robust and efficient cartesian mesh generation for component-based geometry, January 1997, AIAA Paper 97-0196.
23. NEMEC, M., AFTOSMIS, M.J. and WINTZER, M. Adjoint-based adaptive mesh refinement for complex geometries, AIAA 2008-0725.
24. CHADERJAN, N.M., ROGERS, S.E., AFTOSMIS, M.J., PANDYA, S.A., AHMAD, J.U. and TEJNIL, E. Automated Euler and Navier-Stokes database generation for a glide-back booster, July 2004, Third International Conference on Computational Fluid Dynamics, Toronto, Canada, Springer-Verlag.
25. WINTZER, M., NEMEC, M. and AFTOSMIS, M. Adjoint-based adaptive mesh refinement for sonic boom prediction, AIAA 2008-6593.
26. AFTOSMIS, M.J., NEMEC, M. and CLIFF, S.E. Adjoint-based low-boom design with Cart3D, AIAA 2011-3500.
27. ELMILIGUI, A., CLIFF, S., WILCOX, F. and THOMAS S. Numerical predictions of sonic boom signatures for a straight line segmented leading edge model, 2012, ICCFD7-2004.
28. Star-CCM+, CFD Software Package, CD-adapco, Melville, New York, USA.
29. <http://www.cd-adapco.com/products/star-ccm-plus>.
30. MENTER, F.R. Two-equation eddy-viscosity turbulence modeling for engineering applications, *AIAA J*, 1994, **32**, (8), pp 1598-1605.
31. DURBIN, P.A. On the *k-e* stagnation point anomaly, *Int J Heat and Fluid Flow*, 1996, **17**, pp 89-90.
32. SHANKARA, P. and SNYDER, D. Numerical simulation of high lift trap wing using STAR-CCM+, AIAA 2012-2920.
33. HANKE, C.R. and NORDWALL, D.R. The simulation of a jumbo-jet transport aircraft, Vol 2, Modeling Data, 1970, NASA CR-114494.
34. MAIR, W.A. and BIRDSALL, D.L. *Aircraft Performance*, 1992, Cambridge University Press, pp 253-257.
35. STRIEPE, S.A., POWELL, R.W., DESAI, P.N., QUEEN, E.M., BRAUER, G.L., CORNICK, D.E., OLSON, D.W., PETERSEN, F.M., STEVENSON, R., ENGEL, M.C., MARSH, S.M. and GROMOKO, A.M. Program to Optimize Simulated Trajectories (POST II), Vol II Utilization Manual Version 1.1.6.G, January 2004, NASA Langley Research Center, Hampton, VA, USA.